INTERNATIONAL JOURNAL FOR NUMERICAL METHODS IN FLUIDS
Int. J. Numer. Meth. Fluids 2007; **53**:1267–1296
Published online 18 April 2006 in Wiley InterScience (www.interscience.wiley.com). DOI: 10.1002/fld.1223

Electromagnetic scattering simulation using an **H**(curl) conforming *hp* finite element method in three dimensions

P. D. Ledger[1,*,†], K. Morgan[2,‡] and O. Hassan[2,§]

[1]*Center for Computational Physics, Zürcher Hochschule Winterthur, Postfach 805, 8401 Winterthur, Switzerland*
[2]*Civil and Computational Engineering Centre, School of Engineering, University of Wales Swansea, Swansea SA2 8PP, U.K.*

SUMMARY

This work describes an approach to solving electromagnetic scattering problems in three dimensions using arbitrary order tetrahedral **H**(curl) conforming finite elements. We use geometric refinement of the grid to isolate the effect of singularities and use non-uniform polynomial degree to reduce the number of unknowns. Initial distributions of the polynomial degree are generated automatically through the use of a dispersion relationship. The large complex linear system is solved efficiently by using a parallel linear equation solver. Both bistatic and monostatic scattering examples are presented to demonstrate the capabilities of the approach. Copyright © 2006 John Wiley & Sons, Ltd.

KEY WORDS: electromagnetic scattering; *hp* finite elements; unstructured meshes

1. INTRODUCTION

Over the last few years, considerable developments have been made in the application of the *hp* finite element method to the solution of problems involving scattering of a plane electromagnetic wave by a general body. These problems are of particular interest to the aerospace industry, where designers need to be able to predict the radar signature of new aircraft configurations. In this context, the development of a capability for simulating problems involving complex three-dimensional scatterer, with small-scale and multi-material features, illuminated by short waves, is a goal that computational scientists have been striving to achieve.

*Correspondence to: P. D. Ledger, Center for Computational Physics, Zürcher Hochschule Winterthur, Postfach 805, 8401 Winterthur, Switzerland.
†E-mail: lep@zhwin.ch
‡E-mail: k.morgan@swansea.ac.uk
§E-mail: o.hassan@swansea.ac.uk

Received 4 October 2005
Revised 7 February 2006
Accepted 16 February 2006

In the past few years, we have been interested in applying *hp* finite element technology to the electromagnetic scattering problem. The approach followed is to use **H**(curl) conforming elements, of the type originally proposed by Nédélec [1–3] and elements of this type have been widely used in the engineering community [4]. Ledger *et al.* [5] used the hierarchical **H**(curl) conforming basis developed by Ainsworth and Coyle [6] for the solution of two-dimensional scattering problems. The radiation condition at the far field was simulated by the use of a perfectly matched layer (PML), similar to that originally proposed by Berenger [7] in the context of the finite difference method. The approach was subsequently extended by the addition of an error estimation procedure, which enabled bounds to be placed on computed outputs of practical interest, such as the distribution of the scattering width [8–10]. Following the development of a three-dimensional hierarchical **H**(curl) conforming basis for unstructured tetrahedral meshes by Ainsworth and Coyle [11], the *hp* finite element approach was applied to large-scale eigenvalue computations [12, 13] and initial investigations of three-dimensional scattering problems were made [14].

In this paper, we wish to present some of our latest results for the solution of the electromagnetic scattering problem in three dimensions, using *hp* version tetrahedral elements. Of direct relevance to this work are the papers by Rachowicz and Zdunek [15, 16], which describe a three-dimensional *hp* finite element approach using hexahedral **H**(curl) conforming elements. This work is similar to the work presented in this paper, but we prefer to use tetrahedral elements, because of the availability of automatic tetrahedral mesh generators and our existing expertise in this area. Although, for the complex configurations, tetrahedral meshes are easier to generate, hexahedral elements are not without their advantages, so that it could be beneficial, in the future, to develop a hybrid mesh procedure. However, in addition to the difference in element types, Rachowicz and Zdunek also prefer to use an infinite element for the simulation of the far-field radiation condition, in contrast to our PML approach. We will also propose a series of novel algorithmic developments, which improve the overall efficiency of the approach.

The presentation of the material proceeds as follows: In Section 2, the strong and weak problem statements for the problem will be given. Then, in Section 3, the finite element basis functions that will be used to obtain an approximate solution to the weak variational statement are provided. In addition, the approach employed for simulations involving curved surfaces will also be discussed. The computational details of the proposed procedure are discussed in Section 4. We complement our description of the approach by providing a series of numerical examples in Section 5. Finally, we close with some concluding remarks.

2. PROBLEM FORMULATION

Consider Maxwell's equations expressed, in the frequency domain for a source-free medium, in the dimensionless form

$$\operatorname{curl}\mathbf{E} = -\mathrm{i}\mu\omega\mathbf{H} \qquad \operatorname{curl}\mathbf{H} = \mathrm{i}\varepsilon\omega\mathbf{E} \tag{1}$$

where **E** and **H** are the electric and magnetic field intensity vectors, respectively, ε and μ are relative material parameters, the frequency is such that $\omega^2 > 0$ and $\mathrm{i}^2 = -1$. It is convenient

to split the electric and magnetic fields in the form

$$\mathbf{E} = \mathbf{E}^{\text{sca}} + \mathbf{E}^{\text{inc}} \qquad \mathbf{H} = \mathbf{H}^{\text{sca}} + \mathbf{H}^{\text{inc}} \tag{2}$$

where the superscripts 'inc' and 'sca' refer to the (known) incident and the scattered field components, respectively. The incident fields are assumed to be generated by a source located in the far field and satisfy Maxwell's equations in free space, so that

$$\operatorname{curl} \mathbf{E}^{\text{inc}} = -\mathrm{i}\omega \mathbf{H}^{\text{inc}} \qquad \operatorname{curl} \mathbf{H}^{\text{inc}} = \mathrm{i}\omega \mathbf{E}^{\text{inc}} \tag{3}$$

Relative to a Cartesian (x, y, z) coordinate system, we write $\mathbf{E} = (E_x, E_y, E_z)^{\mathrm{T}}$ and $\mathbf{H} = (H_x, H_y, H_z)^{\mathrm{T}}$. The problem to be considered is illustrated schematically in Figure 1 and consists of determining the scattered fields which are obtained following the interaction between the incident field and a perfectly conducting obstacle, which is surrounded by free space. This problem is chosen for illustration purposes and it should be noted that the procedure which will be described is readily extendable to deal with problems involving more general, multi-layered scatterers. When the scatterer is a perfect magnetic conductor, the Neumann boundary condition

$$\mathbf{n} \wedge \operatorname{curl} \mathbf{E}^{\text{sca}} = -\mathbf{n} \wedge \operatorname{curl} \mathbf{E}^{\text{inc}} \tag{4}$$

must be applied at the boundary, Γ_{neu}. For a perfect electrical conductor, the Dirichlet condition

$$\mathbf{n} \wedge \mathbf{E}^{\text{sca}} = -\mathbf{n} \wedge \mathbf{E}^{\text{inc}} \tag{5}$$

must be applied at the surface, Γ_{dir}. A radiation condition of the form

$$\lim_{r \to \infty} (\mathbf{r} \wedge \operatorname{curl} \mathbf{E}^{\text{sca}} - \mathrm{i}\omega \mathbf{E}^{\text{sca}}) = 0 \tag{6}$$

is also required to ensure the correct behaviour of the fields at infinity. Combining the curl equations (1) and (2), it follows that the scattered electric field satisfies the vector wave equation

$$\operatorname{curl} \operatorname{curl} \mathbf{E}^{\text{sca}} - \omega^2 \mathbf{E}^{\text{sca}} = \mathbf{0} \tag{7}$$

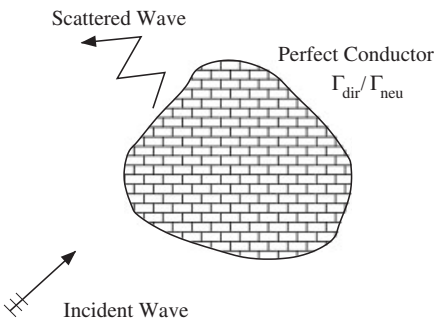

Figure 1. Illustration of the electromagnetic scattering problem.

A similar elimination procedure can also be followed for the magnetic field. However, we choose to develop a solution procedure for the electric field and recover the magnetic field, when required, from Equation (1).

In strong form, the problem may then be stated as: find $\mathbf{E}^{\text{sca}}$ such that

$$\begin{aligned} \operatorname{curl}\operatorname{curl}\mathbf{E}^{\text{sca}} - \omega^2\mathbf{E}^{\text{sca}} &= \mathbf{0} && \text{in } \Omega \\ \mathbf{n}\wedge\operatorname{curl}\mathbf{E}^{\text{sca}} &= -\mathbf{n}\wedge\operatorname{curl}\mathbf{E}^{\text{inc}} && \text{on } \Gamma_{\text{neu}} \\ \mathbf{n}\wedge\mathbf{E}^{\text{sca}} &= -\mathbf{n}\wedge\mathbf{E}^{\text{inc}} && \text{on } \Gamma_{\text{dir}} \\ \lim(\mathbf{r}\wedge\operatorname{curl}\mathbf{E}^{\text{sca}} - \mathrm{i}\omega\mathbf{E}^{\text{sca}}) &= \mathbf{0} && \text{as } r\to\infty \end{aligned} \tag{8}$$

However, with a finite element solution procedure in mind, we consider the corresponding weak variational statement [8]: find $\mathbf{E}^{\text{sca}}\in\mathbf{H}(\operatorname{curl};\Omega)$ such that

$$\begin{gathered} (\operatorname{curl}\mathbf{E}^{\text{sca}},\operatorname{curl}\mathbf{W})_\Omega - \omega^2(\mathbf{E}^{\text{sca}},\mathbf{W})_\Omega = \ell(\mathbf{W}) \quad \forall\mathbf{W}\in\mathbf{H}_0(\operatorname{curl};\Omega) \\ \mathbf{E}^{\text{sca}} + \mathbf{E}^{\text{inc}} \in \mathbf{H}_0(\operatorname{curl};\Omega) \end{gathered} \tag{9}$$

Here, $(\cdot,\cdot)_\Omega$ denotes the standard L^2 inner product over Ω and

$$\ell(\mathbf{W}) = \int_{\Gamma_{\text{neu}}} \mathbf{W}\cdot\mathbf{n}\wedge\operatorname{curl}\mathbf{E}^{\text{inc}}\,\mathrm{d}s \tag{10}$$

is a linear form. The function spaces $\mathbf{H}_0(\operatorname{curl};\Omega)$ and $\mathbf{H}(\operatorname{curl};\Omega)$ employed here are defined as

$$\mathbf{H}_0(\operatorname{curl};\Omega) = \{\mathbf{v},\ \mathbf{v}\in\mathbf{H}(\operatorname{curl};\Omega)\ \mathbf{n}\wedge\mathbf{v}=\mathbf{0},\ \text{on } \Gamma_{\text{dir}}\} \tag{11}$$

and

$$\mathbf{H}(\operatorname{curl};\Omega) = \{\mathbf{v}\in(L^2(\Omega))^3,\ \operatorname{curl}\mathbf{v}\in(L^2(\Omega))^3\} \tag{12}$$

To achieve an approximate numerical solution to this problem, the continuous $\mathbf{H}(\operatorname{curl})$ spaces are replaced by their discrete counterparts. In particular, the discrete spaces $X_H^0\subset\mathbf{H}_0(\operatorname{curl};\Omega)$ and $X_H\subset\mathbf{H}(\operatorname{curl};\Omega)$, are employed together with the discrete variational statement: find $\mathbf{E}_H^{\text{sca}}\in X_H$ such that

$$\begin{gathered} (\operatorname{curl}\mathbf{E}_H^{\text{sca}},\operatorname{curl}\mathbf{W}_H)_\Omega - \omega^2(\mathbf{E}_H^{\text{sca}},\mathbf{W}_H)_\Omega = \ell(\mathbf{W}_H) \quad \forall\mathbf{W}_H\in X_H^0 \\ \mathbf{E}_H^{\text{sca}} + \mathbf{E}^{\text{inc}} \in X_H^0 \end{gathered} \tag{13}$$

To construct an approximate numerical solution, an appropriate finite element discretization must be employed.

3. FINITE ELEMENT DISCRETIZATION

We consider, initially, how a hierarchical $\mathbf{H}(\operatorname{curl})$ conforming discretization may be constructed for use with the weak variational statement of Equation (13). Details will then be given of how the geometry of a general scattering obstacle may be accurately represented.

3.1. Hierarchical finite element basis

High-order **H**(curl) conforming tetrahedral finite elements have been constructed in a variety of different ways [4]. We choose to employ the hierarchical **H**(curl) conforming tetrahedral basis of Ainsworth and Coyle [11], which enables the use of elements of arbitrary order. In this implementation, the basis functions are defined in terms of Legendre polynomials, which lead to relatively well-conditioned matrices [6]. Inside an element, the scattered electric field is approximated as

$$\hat{\mathbf{E}}_H^{\mathrm{sca}} = \sum_{e=1}^{6}\sum_{\ell=0}^{p_e}\hat{\boldsymbol{\phi}}_{\ell}^{e}u_{\ell}^{e} + \sum_{f=1}^{4}\sum_{e\subset\partial f}^{3}\sum_{\ell=0}^{p_f-2}\hat{\boldsymbol{\phi}}_{e,\ell}^{pf}u_{e,\ell}^{pf} + \sum_{f=1}^{4}\underbrace{\sum_{\ell=0}^{p_f-3}\sum_{m=0}^{p_f-3}}_{\ell+m\leqslant p_f-3}(\hat{\boldsymbol{\phi}}_{i,\ell m}^{gf}u_{i,\ell m}^{gf} + \hat{\boldsymbol{\phi}}_{j,\ell m}^{gf}u_{j,\ell m}^{gf})$$

$$+\sum_{f=1}^{4}\underbrace{\sum_{\ell=0}^{p_i-3}\sum_{m=0}^{p_i-3}}_{\ell+m\leqslant p_i-3}\hat{\boldsymbol{\phi}}_{f,\ell m}^{t}u_{f,\ell m}^{t} + \sum_{d=1}^{3}\underbrace{\sum_{\ell=0}^{p_i-4}\sum_{m=0}^{p_i-4}\sum_{n=0}^{p_i-4}}_{\ell+m+n\leqslant p_i-4}\hat{\boldsymbol{\phi}}_{d,\ell mn}^{t}u_{d,\ell mn}^{t} \tag{14}$$

where p_e, p_f and p_i are the polynomial degrees associated with the edges, faces and interior of the element, respectively. The functions $\hat{\boldsymbol{\phi}}_{\ell}^{e}$, $\hat{\boldsymbol{\phi}}_{i,\ell m}^{pf}$ and $\hat{\boldsymbol{\phi}}_{e,\ell}^{gf}$ represent edge basis functions, pseudo face functions and genuine face functions, respectively, with each function having non-vanishing tangential components on the element interfaces. The functions $\hat{\boldsymbol{\phi}}_{f,\ell m}^{t}$ and $\hat{\boldsymbol{\phi}}_{d,\ell mn}^{t}$ represent pseudo and genuine interior functions, which have vanishing tangential components on the element interfaces. For completeness, full details of these basis functions is provided in Table I. These functions are defined for a reference tetrahedron, with vertices $(-1,0,0)$, $(1,0,0)$, $(0,\sqrt{3},0)$ and $(0,\sqrt{3}/3,2\sqrt{2}/\sqrt{3})$, and employ the area coordinates

$$\begin{aligned}\hat{\lambda}_1 &= 1/2 - \xi/2 - \sqrt{3}\eta/6 - \sqrt{6}\zeta/12, \quad \hat{\lambda}_2 = 1/2 + \xi/2 - \sqrt{3}\eta/6 - \sqrt{6}\zeta/12\\ \hat{\lambda}_3 &= \sqrt{3}\eta/3 - \sqrt{6}\zeta/12, \quad \hat{\lambda}_4 = \sqrt{6}\zeta/4\end{aligned} \tag{15}$$

The definition of two sets of edge directions on the reference tetrahedron and its related faces allows the problem of rotational invariance to be dealt with effectively. Without this technique, it is difficult to apply tangential continuity, due to the appearance of conflicting directions on the faces of adjacent tetrahedra. Correctly identifying each element as one of these two types ensures that this problem is avoided [11].

3.2. Geometry resolution

For general scattering obstacles, an accurate geometry representation may be achieved, on arbitrary meshes, by employing edge and face corrections to an otherwise flat boundary face [13]. In this approach, flat tetrahedral faces in the interior of the mesh remain unaltered and the geometry corrections on the curved surfaces are interpolated by the H^1 conforming functions shown in Table I. The amount of correction that is applied depends upon the degree of the interpolating polynomials. With the edge and face corrections, the interpolated geometry is represented in the form

$$\mathbf{x} = \sum_{i=1}^{4}\hat{\lambda}_i\mathbf{x}_i + \sum_{e=1}^{6}\mathbf{x}_e + \sum_{f=1}^{4}\mathbf{x}_f \tag{16}$$

Table I. Ainsworth and Coyle's [11] element basis functions for discrete subspaces $Z_H \subset H^1(\Omega)$ and $X_H \subset \mathbf{H}(\mathrm{curl})$. The functions are grouped by the tetrahedral entity with which they are associated, with $f \backslash e$ representing the vertex in the face $\mathbf{f}$ not on edge $\mathbf{e}$ and $\mathbf{t} \backslash \mathbf{f}$ representing the vertex in the tetrahedron $\mathbf{t}$ not in the face $\mathbf{f}$. The functions L_p are the Legendre polynomials of order p and $\hat{\beta}_{\mathbf{e}} = \hat{\lambda}_o \hat{\lambda}_i$, $\hat{\beta}_{\mathbf{f}} = \hat{\lambda}_o \hat{\lambda}_i \hat{\lambda}_j$ and $\hat{\beta}_{\mathbf{t}} = \hat{\lambda}_o \hat{\lambda}_i \hat{\lambda}_j \hat{\lambda}_k$ are bubble functions associated with an edge, face and tetrahedron, respectively. The vector $\hat{\boldsymbol{\tau}}^{[o\ i]}$ is the unit tangent to the edge $[o\ i]$ and $\hat{\mathbf{e}}_d$ is the unit vector in the d direction.

Associated entity	H^1 conforming	$\mathbf{H}(\mathrm{curl})$ conforming
Vertex	$\hat{\psi}^{\mathbf{v}} = \hat{\lambda}_{\mathbf{v}}$	—
Edge	$\hat{\psi}^{\mathbf{e}}_{\ell} = \hat{\beta}_{\mathbf{e}} L_\ell(\hat{\xi}_{oi})$	$\hat{\boldsymbol{\phi}}^e_0 = \hat{\lambda}_i \hat{\nabla} \hat{\lambda}_o - \hat{\lambda}_o \hat{\nabla} \hat{\lambda}_i,\ \hat{\boldsymbol{\phi}}^e_1 = \hat{\lambda}_i \hat{\nabla} \hat{\lambda}_o + \hat{\lambda}_o \hat{\nabla} \hat{\lambda}_i$
$\mathbf{e} = [o\ i]$	$0 \leqslant \ell \leqslant p_e - 2$	$\hat{\boldsymbol{\phi}}^e_{\ell+1} = \frac{2\ell+1}{\ell+1} L_\ell(\hat{\xi}_{oi}) \hat{\boldsymbol{\phi}}^e_1 - \frac{\ell}{\ell+1} L_{\ell-1}(\hat{\xi}_{oi}) \hat{\boldsymbol{\phi}}^e_0$ $1 \leqslant \ell \leqslant p_e - 1$
Face	$\hat{\psi}^f_{\ell m} = \hat{\beta}_{\mathbf{f}} L_\ell(\hat{\xi}_{oi}) L_m(\hat{\xi}_{oj})$	$\hat{\boldsymbol{\phi}}^{pf}_{\mathbf{e},\ell} = \hat{\beta}_{\mathbf{e}} L_\ell(\hat{\xi}_{oi}) \hat{\nabla} \hat{\lambda}_{f \backslash e}$
$\mathbf{f} = [o\ i\ j]$	$0 \leqslant \ell, m, \ell + m \leqslant p_f - 3$	$0 \leqslant \ell \leqslant p_f - 2$
		$\hat{\boldsymbol{\phi}}^{gf}_{i,\ell m} = \hat{\beta}_f L_\ell(\hat{\xi}_{oi}) L_m(\hat{\xi}_{oj}) \hat{\boldsymbol{\tau}}^{[o\ i]}$ $0 \leqslant \ell, m, \ell + m \leqslant p_f - 3$
Interior	$\hat{\psi}^t_{\ell mn} = \hat{\beta}_{\mathbf{t}} L_\ell(\hat{\xi}_{oi}) L_m(\hat{\xi}_{oj}) L_n(\hat{\xi}_{ok})$	$\hat{\boldsymbol{\phi}}^t_{\mathbf{f},\ell m} = \hat{\beta}_{\mathbf{f}} L_\ell(\hat{\xi}_{oi}) L_m(\hat{\xi}_{oj}) \hat{\nabla} \hat{\lambda}_{t \backslash f}$
$\hat{\mathbf{t}} = [o\ i\ j\ k]$	$0 \leqslant \ell, m, n, \ell + m + n \leqslant p_i - 4$	$0 \leqslant \ell, m, \ell + m \leqslant p_i - 3$
		$\hat{\boldsymbol{\phi}}^t_{d,\ell mn} = \hat{\beta}_{\mathbf{t}} L_\ell(\hat{\xi}_{oi}) L_m(\hat{\xi}_{oj}) L_n(\hat{\xi}_{ok}) \hat{\mathbf{e}}_d$ $d \in \{1,2,3\};\ 0 \leqslant \ell, m, n, \ell + m + n \leqslant p_i - 4$

where $\mathbf{x}_i = (x_i, y_i, z_i)^{\mathrm{T}}$ are the coordinates of vertex i of the element, $\mathbf{x}_e$ are the edge corrections and $\mathbf{x}_f$ are the face corrections. The procedure employed assumes that a parameterization of the curved surface is known, so that the coefficients of the polynomials for the edge and face corrections can be determined. If a parameterization of the surface is not known, this geometry representation technique may be combined with an approximate representation of the curved surface, e.g. a representation supplied in terms of a G^1 patch [17]. However, the verification of the performance of this type of approach is still the topic of on-going research.

4. COMPUTATIONAL DETAILS

4.1. Incident wave specification

In general, a plane incident electromagnetic wave will have an associated electric field, which may be written in the form

$$\mathbf{E}^{\mathrm{inc}} = \mathbf{p} \exp(\mathrm{i}\mathbf{k} \cdot \mathbf{x}) \tag{17}$$

where the vectors $\mathbf{p}$ and $\mathbf{k}$, defined by

$$\mathbf{k} = \omega \begin{bmatrix} \cos\phi \sin\theta \\ \sin\phi \sin\theta \\ \cos\theta \end{bmatrix} \quad \mathbf{p} = \begin{bmatrix} E_\theta^{\text{inc}} \cos\theta \cos\phi - E_\phi^{\text{inc}} \sin\phi \\ E_\theta^{\text{inc}} \cos\theta \sin\phi + E_\phi^{\text{inc}} \cos\phi \\ -E_\theta^{\text{inc}} \sin\theta \end{bmatrix} \tag{18}$$

are orthogonal. In the above θ and ϕ are the usual spherical polar coordinates. Setting $E_\theta^{\text{inc}} = 0$ and $E_\phi^{\text{inc}} = -1$ defines a wave which is ϕ polarized, while setting $E_\theta^{\text{inc}} = 1$ and $E_\phi^{\text{inc}} = 0$ defines waves which are θ polarized. This, together with the selection of the angles (θ, ϕ), determines the overall polarization of the incident field. For example, for $\theta = \pi/2$, a ϕ polarized incident wave is such that the incident field is parallel to the x axis. This is normally termed a horizontally polarized incident field. Correspondingly, for $\theta = \pi/2$ and a θ polarized wave, we obtain an incident field that is parallel to the y axis. This is normally termed a vertically polarized incident field.

4.2. Dirichlet and Neumann boundary conditions

The application of Neumann boundary conditions is achieved by evaluating the term $\mathbf{n} \wedge \operatorname{curl} \mathbf{E}^{\text{inc}}$, in the linear form $\ell(\mathbf{W})$, using the known field. To apply the Dirichlet boundary conditions, we need to determine the coefficients of the basis associated with the tangential component of the field on the boundary surface. This is complicated, as the basis is made up of edge functions, pseudo and genuine face functions and pseudo and genuine interior functions. The tangential component of the interior basis functions vanish on the boundary surface and, therefore, can be ignored. For the other basis functions, we exploit the hierarchical nature of the basis to apply the boundary conditions. To achieve this, we first solve the system

$$\begin{bmatrix} a_{11}^e & a_{12}^e & \cdots & a_{1(p_e+1)}^e \\ a_{21}^e & a_{22}^e & & \\ \vdots & & \ddots & \\ a_{(p_e+1)1}^e & a_{(p_e+1)2}^e & \cdots & a_{(p_e+1)(p_e+1)}^e \end{bmatrix} \begin{bmatrix} u_1^e \\ u_2^e \\ \vdots \\ u_{(p_e+1)}^e \end{bmatrix} = \begin{bmatrix} r_1^e \\ r_2^e \\ \vdots \\ r_{(p_e+1)}^e \end{bmatrix} \tag{19}$$

on each boundary edge of the surface. Here, the typical entries are

$$a_{ij}^e = \int_e (\boldsymbol{\tau} \cdot \boldsymbol{\phi}_i^e)(\boldsymbol{\tau} \cdot \boldsymbol{\phi}_j^e)\, \mathrm{d}s_e \quad r_i^e = -\int_e (\boldsymbol{\tau} \cdot \boldsymbol{\phi}_i^e)(\boldsymbol{\tau} \cdot \mathbf{E}^{\text{inc}})\, \mathrm{d}s_e \tag{20}$$

and u_i^e denotes the unknown associated with the edge basis function $\boldsymbol{\phi}_i^e$. The block system

$$\begin{bmatrix} \mathbf{A}^{pf} & \mathbf{C}^f \\ (\mathbf{C}^f)^{\mathrm{T}} & \mathbf{A}^{gf} \end{bmatrix} \begin{bmatrix} \mathbf{u}^{pf} \\ \mathbf{u}^{gf} \end{bmatrix} = \begin{bmatrix} \mathbf{r}^{pf} \\ \mathbf{r}^{gf} \end{bmatrix} \tag{21}$$

is then solved on each face of the boundary surface. Here, typical entries in the matrices are

$$a_{ij}^{pf} = \int_f (\mathbf{n} \wedge \boldsymbol{\phi}_i^{pf}) \cdot (\mathbf{n} \wedge \boldsymbol{\phi}_j^{pf}) \, \mathrm{d}s_f \tag{22}$$

$$c_{ij}^{f} = \int_f (\mathbf{n} \wedge \boldsymbol{\phi}_i^{pf}) \cdot (\mathbf{n} \wedge \boldsymbol{\phi}_j^{gf}) \, \mathrm{d}s_f \tag{23}$$

$$a_{ij}^{gf} = \int_f (\mathbf{n} \wedge \boldsymbol{\phi}_i^{gf}) \cdot (\mathbf{n} \wedge \boldsymbol{\phi}_j^{gf}) \, \mathrm{d}s_f \tag{24}$$

$$r_i^{pf} = \int_f \mathbf{n} \wedge \left(-\mathbf{E}^{\mathrm{inc}} - \sum_{e \in f} \sum_{j=1}^{p_e+1} u_j^e \boldsymbol{\phi}_j^e \right) \cdot (\mathbf{n} \wedge \boldsymbol{\phi}_i^{pf}) \, \mathrm{d}s_f \tag{25}$$

$$r_i^{gf} = \int_f \mathbf{n} \wedge \left(-\mathbf{E}^{\mathrm{inc}} - \sum_{e \in f} \sum_{j=1}^{p_e+1} u_j^e \boldsymbol{\phi}_j^e \right) \cdot (\mathbf{n} \wedge \boldsymbol{\phi}_i^{gf}) \, \mathrm{d}s_f \tag{26}$$

The coefficients in $\mathbf{u}^{pf} = [u_1^{pf}, \ldots, u_{3(p_f-1)}]^{\mathrm{T}}$ and $\mathbf{u}^{gf} = [u_1^{gf}, \ldots, u_{(p_f-1)(p_f-2)}^{gf}]^{\mathrm{T}}$ are associated with pseudo and genuine face functions, respectively. The computation of the Dirichlet coefficients for the edge basis functions may be separated from the computation of the face basis functions, as the tangential component of the face basis functions vanishes on the edges of the faces. The face basis functions can be viewed as bubble functions which correct the tangential component of the field on the interior of a face. Following the solution of this matrix system, all the information required to apply the Dirichlet boundary conditions is available.

To investigate the accuracy of this form of boundary condition application, we consider a simple example involving the propagation of the plane wave

$$\mathbf{E} = [0, 0, 1]^{\mathrm{T}} \exp(\mathrm{i}\omega x) \tag{27}$$

with $\omega = 2\pi$, across a unit square. The error, $\|\mathbf{e}\|_{H_c}$, in the $\mathbf{H}(\mathrm{curl})$ norm is defined as

$$\|\mathbf{e}\|_{H_c}^2 = \|\mathbf{E} - \mathbf{E}_H\|_{H_c}^2 = \int_\Omega (\|\mathbf{E} - \mathbf{E}_H\|_2^2 + \|\mathrm{curl}(\mathbf{E} - \mathbf{E}_H)\|_2^2) \, \mathrm{d}\Omega \tag{28}$$

where $\| \cdot \|_2$ is the standard Euclidean norm. We compute $\|\mathbf{e}\|_{H_c}$ for a number of simulations using a uniform polynomial, or p, refinement of an initial mesh. The variation of the computed error with increasing polynomial order, when either Neumann or Dirichlet boundary conditions are applied, is shown in Figure 2. Here, each point on the curve represents a discretization with increasing polynomial order. The correct exponential convergence behaviour may be observed, for both Dirichlet and Neumann boundary conditions, at high p. This is an important property for electromagnetic scattering simulations, which frequently require the application of Dirichlet boundary conditions at the surface of a perfect electrical conductor.

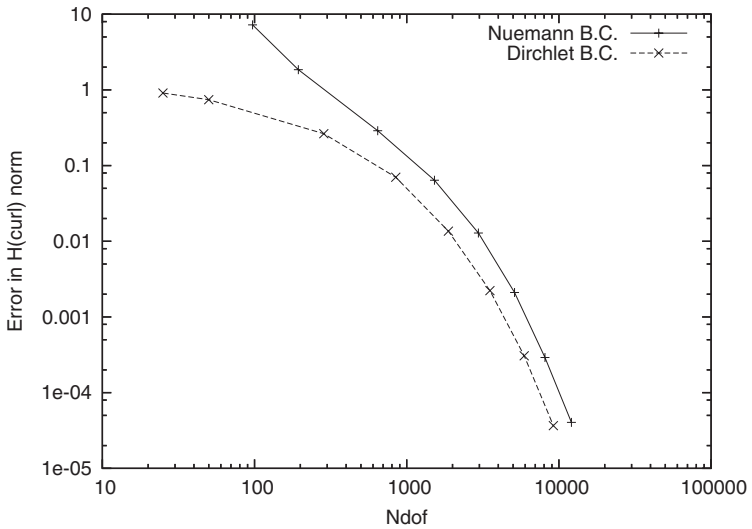

Figure 2. Simulation of the propagation of a plane wave on a unit square showing the error in the **H**(curl) norm when either Dirichlet or Neumann boundary conditions are applied.

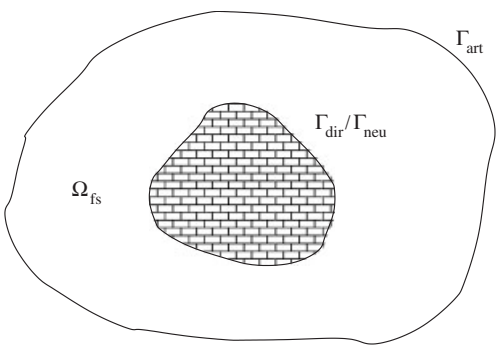

Figure 3. Introduction of an artificial boundary, Γ_{art}, creating a finite computational domain, Ω_{fs}.

4.3. Far-field boundary condition

Before the numerical simulation of the scattering problem can be attempted, the infinite physical domain must be truncated in some manner. Usually, an artificial numerical boundary Γ_{art} is located at some finite distance from the scatterer and the problem is solved in the finite computational domain between the scatterer and the artificial boundary, as shown in Figure 3. An accurate simulation demands an accurate modelling of the effects of the outgoing scattered wave at the artificial boundary and a range of different methods have been proposed for achieving this. Typical candidate methods include coupling the finite element technique with a boundary element method (BEM) [18, 19], the use of a Dirichlet to Neumann (DtN)

map [20, 21], the use of infinite elements [22], the use of an absorbing boundary condition (ABC) and approximation by the addition of a PML [7, 23, 24]. When selecting from this list of possibilities, consideration should be given to the ease of implementation, the accuracy of the representation of the scattered field within the truncated domain and the additional computational expense which is introduced by employing the boundary condition.

The use of a BEM or a DtN technique certainly offers the possibility of high levels of numerical accuracy. In these approaches, the decay of the scattered wave in the infinite domain is correctly modelled and the artificial boundary may be placed very close to the scatterer. However, both approaches involve a high additional computational cost. The BEM requires the solution of a full linear system, while the implementation of the DtN approach may also destroy the structure of the sparse matrix resulting from the finite element discretization. Both the BEM and DtN approaches require the evaluation of complex integrals involving Hankel functions. Infinite elements involve the addition of special finite elements which extend to infinity. Integrals involving Hankel functions again arise although, in the approach employed by Zdunek and Rachowicz [15, 16], these complex expressions may be evaluated analytically [25]. A good approximation of the far-field behaviour is obtained, but the terms in the truncated infinite series can be expensive to evaluate and large matrices, with high condition numbers, can appear. On the other hand, an ABC is relatively cheap, requiring only the evaluation of a boundary integral involving the basis functions on the artificial boundary. Depending upon the choice of the artificial boundary, and the basis functions employed, the symmetric nature of the linear system remains or is destroyed. The biggest disadvantage of the ABC approach is that the boundary must normally be placed at considerable distance from the scatterer, in order to achieve high levels of accuracy, especially when problems with high frequencies are considered. The PML of Berenger [7] makes an attractive alternative, as the artificial boundary can be placed relatively close to the object and good levels of accuracy can be obtained. The method is implemented by the addition of an artificial layer Ω_{pml}, with suitably defined material coefficients, to the outside of the truncated domain, as illustrated in Figure 4. In this work, the PML implementation of Sacks *et al.* [23] is followed, in which the artificial layer

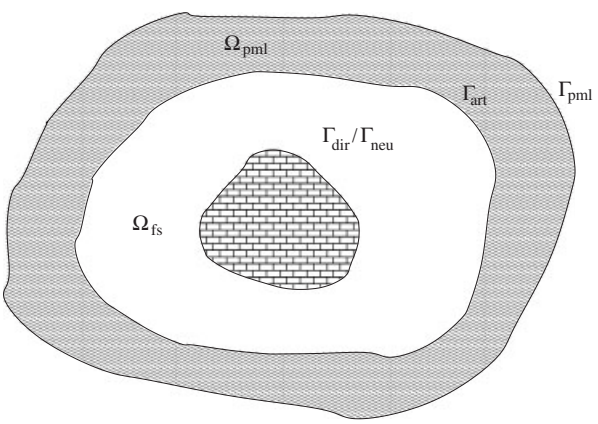

Figure 4. Addition of a PML, Ω_{pml}, to the outside of the computational domain.

takes the form of a rectangular box, with material coefficients

$$\mu = \varepsilon = \begin{bmatrix} s_y s_z s_x^{-1} & 0 & 0 \\ 0 & s_x s_z s_y^{-1} & 0 \\ 0 & 0 & s_x s_y s_z^{-1} \end{bmatrix} \tag{29}$$

where

$$s_x = \begin{cases} 1 + \mathrm{i}\sigma_x/\omega & \text{for } x \geqslant x_{\text{art}}^+ \\ 1 + \mathrm{i}\sigma_x/\omega & \text{for } x \leqslant x_{\text{art}}^- \\ 1 & \text{otherwise} \end{cases} \tag{30}$$

$$s_y = \begin{cases} 1 + \mathrm{i}\sigma_y/\omega & \text{for } y \geqslant y_{\text{art}}^+ \\ 1 + \mathrm{i}\sigma_y/\omega & \text{for } y \leqslant y_{\text{art}}^- \\ 1 & \text{otherwise} \end{cases} \tag{31}$$

$$s_z = \begin{cases} 1 + \mathrm{i}\sigma_z/\omega & \text{for } z \geqslant z_{\text{art}}^+ \\ 1 + \mathrm{i}\sigma_z/\omega & \text{for } z \leqslant z_{\text{art}}^- \\ 1 & \text{otherwise} \end{cases} \tag{32}$$

and $(x_{\text{art}}^-, y_{\text{art}}^-, z_{\text{art}}^-) \times (x_{\text{art}}^+, y_{\text{art}}^+, z_{\text{art}}^+)$ defines the rectangular boundary Γ_{art} containing the free space region. In the anisotropic PML approach, the scattered field satisfies the modified vector wave equation

$$\operatorname{curl} \mu^{-1} \operatorname{curl} \mathbf{E}_H^{\text{sca}} - \omega^2 \varepsilon \mathbf{E}_H^{\text{sca}} = \mathbf{0} \quad \text{in } \Omega_{\text{pml}} \tag{33}$$

The absorption coefficients σ_x, σ_y and σ_z are defined in the form

$$\sigma(t) = (t/d)^m \sigma_{\max} \tag{34}$$

where t is a distance coordinate, measured in the appropriate coordinate direction from the inside of the PML, and $t = d$ at the outer boundary, Γ_{pml}. The thickness of the layer, the discretization of the layer and the value of $\sigma_{\max}$ have to be selected for a practical implementation. Using low-order approximations, problems have been encountered when too few elements are used within the PML layer, as this results in large jumps in the material coefficients from element to element. However, this is not so important with an *hp* approach, as the nature of the high-order elements means that the transition of the material coefficients between one element and the next is well modelled as the order of the elements is increased. The approach described by Taflove [26] is used to select the coefficient $\sigma_{\max}$ and the thickness of the PML layer is set to be a small fraction of the wavelength. Further improvements in the quality of the PML can be achieved by additionally imposing a first-order ABC at the outer surface Γ_{pml} [19]. The advantages of this approach were first reported by Collino and Monk [27] and, following our earlier success with this approach in two dimensions [8], the approach

is also adopted here. In this case, the approximate variational statement is now modified to read: find $\mathbf{E}_H^{\text{sca}} \in X_H$ such that

$$(\mu^{-1}\operatorname{curl}\mathbf{E}_H^{\text{sca}}, \operatorname{curl}\mathbf{W}_H)_{\Omega_{fs}+\Omega_{\text{pml}}} - \omega^2(\varepsilon\mathbf{E}_H^{\text{sca}}, \mathbf{W}_H)_{\Omega_{fs}+\Omega_{\text{pml}}} + b(\mathbf{E}_H^{\text{sca}}, \mathbf{W}) = \ell(\mathbf{W}_H) \quad \forall \mathbf{W}_H \in X_H^0$$
$$\mathbf{E}_H^{\text{sca}} + \mathbf{E}^{\text{inc}} \in X_H^0 \tag{35}$$

where

$$b(\mathbf{u}, \mathbf{v}) = \mathrm{i}\omega \int_{\Gamma_{\text{pml}}} (\mathbf{n} \wedge \mathbf{u}) \cdot (\mathbf{n} \wedge \mathbf{v}) \, \mathrm{d}s \tag{36}$$

is the first-order approximate boundary condition applied on the exterior surface Γ_{pml}. The value of ε and μ in Ω_{pml} are defined by Equation (29), with the corresponding values in Ω_{fs} are set equal to the unit tensor.

4.4. Non-uniform p-distribution

Solutions to problems involving sharp corners and edges will exhibit strong singularities in the neighbourhood of these features. It is advisable to employ small, low-order elements around corners and edges, to localize the effects of these singularities. In regions where the solution is smooth, larger, high-order elements can be used. This implies that we must allow for elements of different polynomial order in different regions of the domain and this is accomplished by the use of the minimum rule. This rule requires that the polynomial degree on two neighbouring faces, or edges, should be selected to be the minimum of that of the two neighbouring entities. In addition, the polynomial degree on an edge cannot exceed that on a face, while the polynomial degree on a face cannot exceed that in the interior of an element, i.e. $p_e \leqslant p_f \leqslant p_i$.

In practice, to achieve an accurate solution, the element order and the element size must be sufficient to ensure that the field can be well represented. Here, well represented means that the interpolation error (i.e. the representation of the continuous function by a discrete function) and the dispersion error (i.e. the phase difference between the exact and computed wave) must be sufficiently well resolved. The interpolation error can be controlled by refining the discretization but, to control dispersion, we need to ensure that the discretization is such that the difference between the actual and the computed wave number is small. On a given mesh, we normally follow an approach in which the initial distribution of the polynomial order is determined from the dispersion relationship produced for hierarchical $\mathbf{H}(\text{curl})$ conforming hexahedra by Ainsworth [28]. For $\omega h \leqslant 1$ the relationship may be written in the form

$$\omega^2 - \left(\xi_x^2 + \xi_y^2 + \xi_z^2 + \frac{h^{2(p+1)}}{2(p+1)+1} \left(\frac{(p+1)!}{(2(p+1))!} \right)^2 (\xi_x^{2(p+1)+2} + \xi_y^{2(p+1)+2} + \xi_z^{2(p+1)+2}) \right)$$
$$= O(h^{2(p+1)+2}) \tag{37}$$

where (ξ_x, ξ_y, ξ_z) is the computed wave number. In regions where $\omega h \gg 1$ it has been conjectured [28] that the dispersion is under control when $2p + 1 \geqslant \omega h$. There is, currently, no equivalent relationship for tetrahedral elements and, therefore, the dispersion relationship for

the hexahedral elements is used as an approximate indicator here. In practice, to generate the initial distribution of p, we follow the steps outlined in Algorithm 1.

Algorithm 1
Allocating a polynomial order to each element on an initial mesh using the dispersion relationship.

for $i = 1$, *Number of Elements* **do**
  Compute the element size, h;
  Compute the polynomial order required to overcome dispersion using either Equation (37) or the rule $2p + 1 \geqslant \omega h$;
  Set $p_i = p$;
end
for $f = 1$, *Number of Faces* **do**
  Set the polynomial order p_f on the face f to be minimum of the orders in the two neighbouring elements;
end
for $e = 1$, *Number of Edges* **do**
  Set the polynomial order p_e on the edge e to be minimum of the orders in the elements surrounding the edge;
end
Check that the minimum rule $p_e \leqslant p_f \leqslant p_i$ is everywhere satisfied.

4.5. Solution of the linear equation set

Before solution, the size of the linear system is reduced by using static condensation to eliminate the degrees of freedom associated with the interior basis functions of each element [4]. In this approach, the linear system for the degrees of freedom associated with the edges and faces of the mesh is first assembled and solved. The degrees of freedom associated with the interior of the elements are then obtained in a second step. The assembly of the stiffness matrix has been parallelized using OpenMP and the parallel linear solver Pardiso [29, 30] is employed for the solution of the linear system. Pardiso is a robust and memory efficient linear solver which uses METIS [31] for the partitioning and is capable of handling the complex linear systems of equations which arise in our applications. We note that Paradiso performs well in the extensive numerical experiments undertaken by Gould *et al.* [32].

4.6. Solution visualization

The nature of the *hp* finite element method means that the meshes used in the computations will often consist of very large high-order elements, over which the electromagnetic field may vary considerably, and smaller lower-order elements, in which the solution may have sharp peaks. For visualization, both commercial and non-commercial plotting packages are usually capable of displaying either a linear or a constant variation of the field over each element. To use one of these packages, to display the solution on the scatterer computed with our *hp* approach, we subdivide the high-order surface elements into a number of smaller triangles. We subdivide an equilateral reference triangle, with vertices $(1, 0)$, $(0, \sqrt{3})$ and $(-1, 0)$, and

typical subdivisions are shown in Figure 5. The locations of the vertices of the split reference triangle are then mapped using the affine mapping

$$\begin{bmatrix} \xi \\ \eta \\ \zeta \end{bmatrix} = \sum_{i=1}^{3} \hat{\lambda}_i \begin{bmatrix} \xi_i \\ \eta_i \\ \zeta_i \end{bmatrix} \tag{38}$$

for the face of the reference tetrahedral element which corresponds to the true face, lying on the surface to be visualized. Here, $(\xi_i, \eta_i, \zeta_i)^{\mathrm{T}}$ are the coordinates of the vertex i, contained within the face of the reference tetrahedron. In terms of the reference triangle coordinates $(\hat{\xi}, \hat{\eta})$, the area coordinates are

$$\hat{\lambda}_1 = (\sqrt{3} + \sqrt{3}\hat{\xi} - \hat{\eta})/(2\sqrt{3}) \tag{39}$$

$$\hat{\lambda}_1 = \hat{\eta}/\sqrt{3} \tag{40}$$

$$\hat{\lambda}_3 = (\sqrt{3} + \sqrt{3}\hat{\xi} - \hat{\eta})/(2\sqrt{3}) \tag{41}$$

Note that the elements used only have tangential continuity, so that it is possible to have different field values on neighbouring tetrahedral faces. To overcome this problem, the values are simply averaged for plotting purposes. The coordinates of the new vertices created in the split surface mesh can then be found by applying the mapping of Equation (16). When the surface of the elements on the boundary are flat, this reduces to an affine mapping.

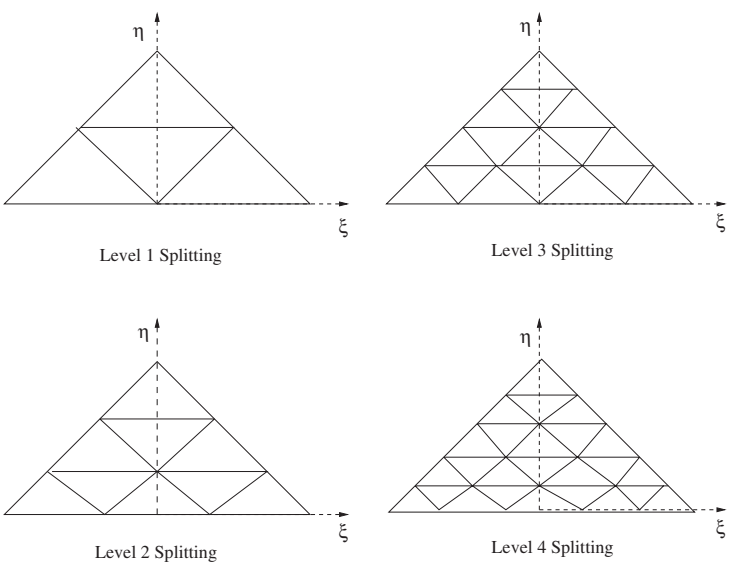

Figure 5. Splitting of the equilateral reference triangle for surface plotting.

As an example, Figure 6(a) shows a coarse mesh on the surface of a sphere, which is used in for the solution process. Figure 6(b) shows the corresponding split mesh, which is used for visualization of the computed solution. In this example, the blending function technique has been used to generate the new vertex coordinates and the edges of the computational mesh are split 10 times. The storage required for the subdivided meshes is minimal, as we are only required to subdivide the faces of the surface mesh where the visualization is required.

4.7. Computation of the radar cross section

The radar cross section, expressed in decibels, $\mathrm{RCS} = 10\log_{10}(\sigma)$, in a scattering simulation may be computed from [26]

$$\sigma(\theta,\phi) = \frac{k^2}{8\pi}(|L_\phi + N_\theta|^2 + |L_\theta - N_\phi|^2) \tag{42}$$

where

$$N_\theta = \int_S (J_x\cos\theta\cos\phi + J_y\cos\theta\sin\phi - J_z\sin\theta)\exp(\mathrm{i}\mathbf{k}\cdot\mathbf{x}')\,\mathrm{d}s' \tag{43}$$

$$N_\phi = \int_S (-J_x\sin\phi + J_y\cos\phi)\exp(\mathrm{i}\mathbf{k}\cdot\mathbf{x}')\,\mathrm{d}s' \tag{44}$$

$$L_\theta = \int_S (M_x\cos\theta\cos\phi + M_y\cos\theta\sin\phi - M_z\sin\theta)\exp(\mathrm{i}\mathbf{k}\cdot\mathbf{x}')\,\mathrm{d}s' \tag{45}$$

$$L_\phi = \int_S (-M_x\sin\phi + M_y\cos\phi)\exp(\mathrm{i}\mathbf{k}\cdot\mathbf{x}')\,\mathrm{d}s' \tag{46}$$

and $\mathbf{M} = -\mathbf{n}\wedge\mathbf{E}^{\mathrm{sca}}$ and $\mathbf{J} = \mathbf{n}\wedge\mathbf{H}^{\mathrm{sca}}$ denote the computed electric current and magnetic current, respectively, on S. The surface S is the collection surface and this may be chosen as any surface which encloses the scatterer and lies in free space. For perfectly conducting scatterers, the surface of the scatterer $\Gamma_{\mathrm{neu}}/\Gamma_{\mathrm{dir}}$ makes a natural choice for S. Following a similar procedure

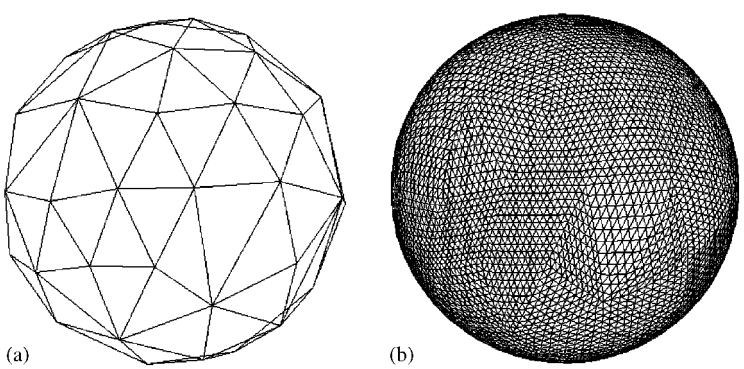

Figure 6. Splitting of the surface of a sphere to enable visualization of the solution: (a) the mesh used for computation; and (b) the split mesh used for displaying the computed solution.

to that of Monk *et al.* [33–35], the accuracy of the computed distribution may be improved by careful computation of N_θ and N_ϕ. This is achieved by evaluating these quantities, in terms of volume integrals, as

$$N_\theta \approx \frac{\mathrm{i}}{\omega}\left(\int \omega^2 \mathbf{E}_H^{\mathrm{sca}} \cdot \mathbf{V}_H - \operatorname{curl} \mathbf{E}_H^{\mathrm{sca}} \cdot \operatorname{curl} \mathbf{V}_H \, \mathrm{d}\Omega'\right) \tag{47}$$

$$N_\phi \approx \frac{\mathrm{i}}{\omega}\left(\int \omega^2 \mathbf{E}_H^{\mathrm{sca}} \cdot \mathbf{Y}_H - \operatorname{curl} \mathbf{E}_H^{\mathrm{sca}} \cdot \operatorname{curl} \mathbf{Y}_H \, \mathrm{d}\Omega'\right) \tag{48}$$

Here,

$$\mathbf{V}_H = \begin{cases} \mathbf{v}_H & \text{on } S \\ \mathbf{0} & \text{in } \Omega' \end{cases} \qquad \mathbf{Y}_H = \begin{cases} \mathbf{y}_H & \text{on } S \\ \mathbf{0} & \text{in } \Omega' \end{cases}$$

while $\mathbf{v}_H$ is the finite element interpolant of $(\cos\theta\cos\phi, \cos\theta\sin\phi, -\sin\theta)\exp(\mathrm{i}\mathbf{k}\cdot\mathbf{x}')$ and $\mathbf{y}_H$ is the finite element interpolant of $(-\sin\theta, \cos\phi, 0)\exp(\mathrm{i}\mathbf{k}\cdot\mathbf{x}')$. Choosing $\mathbf{V}_H$ and $\mathbf{Y}_H$ in this way minimizes the computational cost, as we only required to consider elements directly adjacent to the collection surface.

The direction of the incident wave plays an important role in determining the resulting RCS distribution. When the direction of the incident wave is the same as the angles used for the evaluation of the RCS a single monostatic value of the RCS is obtained. Multiple simulations with different angles must be undertaken to find a complete monostatic profile of the RCS. The polarization of the monostatic RCS is determined by the polarization of the incident wave. Thus, a sequence of horizontally polarized waves result in a horizontally polarized monostatic distribution of the RCS (σ_{HH}) and a sequence of vertically polarized incident waves result in a vertically polarized distribution of the monostatic RCS (σ_{VV}). To enable an efficient an computation of the monostatic RCS distributions, we compute, before the finite element assembly procedure, the coefficients associated with our basis functions for multiple Dirichlet boundary conditions. In particular, one set of coefficients is determined for each of the directions considered in the monostatic RCS distribution. The complex indefinite set of linear equations is then solved for solutions corresponding to the multiple right-hand sides originating from the Dirichlet boundary conditions.

When a single incident wave direction is considered, and the viewing angles used in the RCS expression are varied, a bistatic RCS profile is then obtained. For the bistatic RCS, the polarization of the distribution is obtained by fixing either the θ or the ϕ angles. In this case, care should be taken so the correct combination of θ and ϕ are used. We employ the angles

$$\text{Vertical polarization} = \begin{cases} \theta = 0 \to \pi & \phi = \pi \\ \theta = -\pi \to 0 & \phi = 0 \end{cases}$$

$$\text{Horizontal polarization} = \theta = \pi/2 \quad \phi = -\pi \to \pi$$

for the two polarizations of the bistatic RCS, independent of the direction of the incident wave.

5. NUMERICAL RESULTS

5.1. Bistatic scattering by a 1λ sphere

The first example involves scattering of a plane electromagnetic wave, for which $\theta = \pi/2$, $\phi = 0$, $E_\theta^{\text{inc}} = 0$ and $E_\phi^{\text{inc}} = 1$, by a perfect electrical conducting sphere of diameter 1λ. A mesh of 2506 elements is employed and a view of the surface discretization is displayed in Figure 6(a). Figure 7 shows the bistatic RCS distributions computed when the polynomial order is uniformly increased on this mesh, from $p = 0$ to $p = 4$. It is observed that, as the polynomial order is increased, mesh convergence of the RCS distribution is achieved. In Figure 8, the computed RCS distribution for $p = 4$ elements is compared with the exact Mie Series solution and the agreement is excellent. To investigate the convergence behaviour,

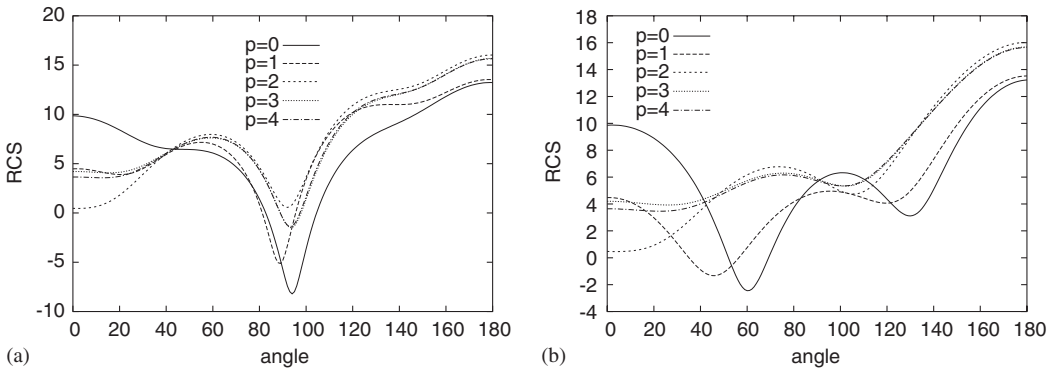

Figure 7. Scattering of a plane electromagnetic wave by a 1λ sphere: the bistatic RCS distributions, computed with uniform polynomial order increase on a fixed mesh for: (a) the vertical polarization; and (b) the horizontal polarization.

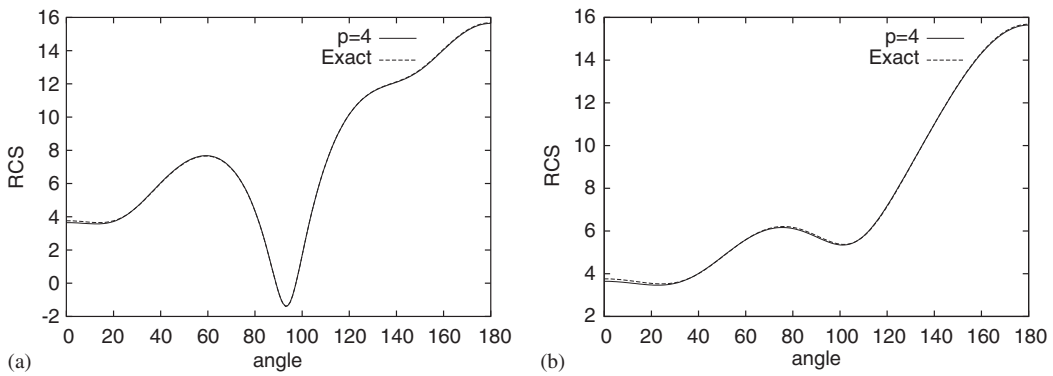

Figure 8. Scattering of a plane electromagnetic wave by a 1λ sphere: comparison between the computed (order $p = 4$) and Mie series bistatic RCS distributions for: (a) the vertical polarization; and (b) the horizontal polarization.

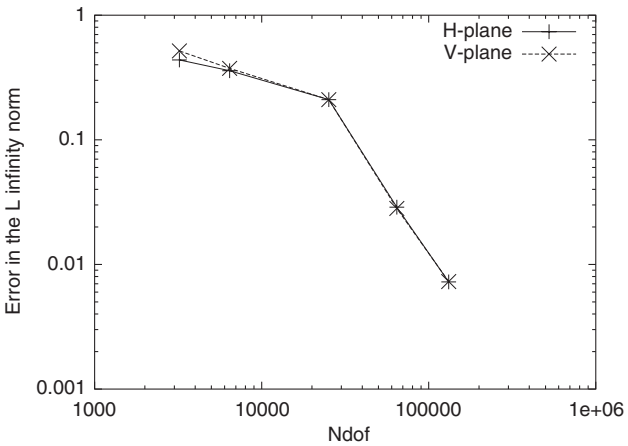

Figure 9. Scattering of a plane electromagnetic wave by a 1λ sphere: convergence of $\|\sigma_H(\theta) - \sigma_{\text{exact}}(\theta)\|_\infty / \|\sigma_{\text{exact}}(\theta)\|_\infty$, for both the vertical and horizontal polarizations, as the number of degrees of freedom is increased due to uniform p refinement.

we monitor the quantity $\|\sigma(\alpha) - \sigma_{\text{exact}}(\alpha)\|_\infty / \|\sigma_{\text{exact}}(\alpha)\|_\infty$ for both the vertical ($\alpha = (\theta = 0 \to \pi, \phi = \pi)$) and horizontal polarizations ($\alpha = (\theta = \pi/2, \phi = 0 \to \pi)$) and the results are displayed in Figure 9. It is apparent that, once the dispersion is brought under control, the RCS distributions converge rapidly. Figure 10 displays the contours of the scattered field components E_x^{sca}, E_y^{sca} and E_z^{sca} on the sphere surface. An indication of the computational efficiency of the parallel algorithm may be obtained from Table II. This compares the performance of the solution algorithm, as the number of processors employed increases from 1 to 6, with the maximum theoretical speed-up. It may be observed that, with up to 4 processors, over 70% of the theoretical speed-up is attained. However, beyond 4 processors, this percentage reduces rapidly. Although these figures represent the overall timing of the complete program, the authors of Pardiso report a speed-up of around 87.5% with certain classes of matrices on 8 processors. Thus, as our observations only apply to the small mesh of 2506 elements, we would expect better parallel efficiency on larger meshes with 8 processors.

5.2. *Bistatic scattering by a* 1λ *cube*

This example involves the scattering of a plane electromagnetic wave, for which $\theta = \pi/2$, $\phi = 0$, $E_\theta^{\text{inc}} = 0$ and $E_\phi^{\text{inc}} = 1$, by a perfect electrical conducting cube of edge length 1λ. The solution is computed on a mesh of 2277 elements, with the surface discretization shown in Figure 11(a), and also on a mesh of 7408 elements, with the surface discretization shown in Figure 11(b). The first mesh has a uniform spacing, while the second mesh exhibits a geometric refinement as the edges and corners of the cube are approached. On each mesh, the convergence of the bistatic RCS distribution is examined as the polynomial order is uniformly increased. We also consider the RCS distribution which is produced when the polynomial order on each element in these meshes is determined according to either the dispersion relationship of Equation (37) or the rule $2p + 1 \geqslant \omega h$. The results for the first mesh

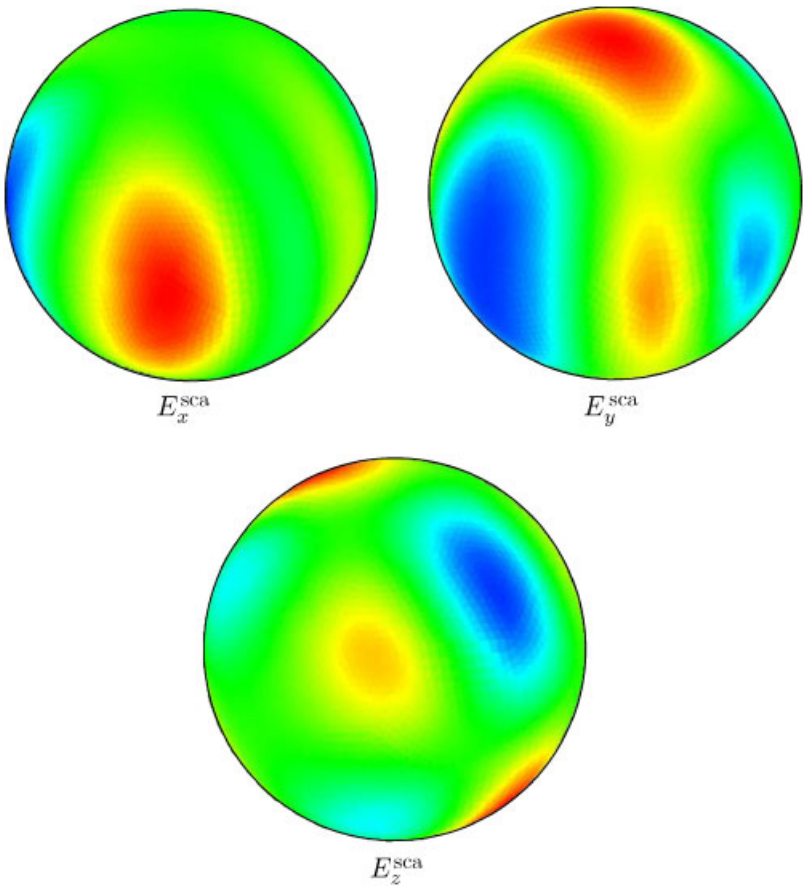

Figure 10. Scattering of a plane electromagnetic wave by a 1λ sphere: the computed contours of E_x^{sca}, E_y^{sca} and E_z^{sca} on the surface of the sphere.

Table II. The percentage speed-up achieved, as the number of processors employed is increased, for the solution of scattering of a plane electromagnetic wave by a 1λ sphere.

Number of processors	Percentage of theoretical speed-up achieved
1	100
2	87.8
3	78.27
4	72.25
5	66.15
6	58.86

are shown in Figure 12 and the distributions computed on the second mesh are shown in Figure 13. It can be observed that, in both cases, the non-uniform polynomial distribution obtained by using Algorithm 1 gives very good agreement with the mesh converged bistatic

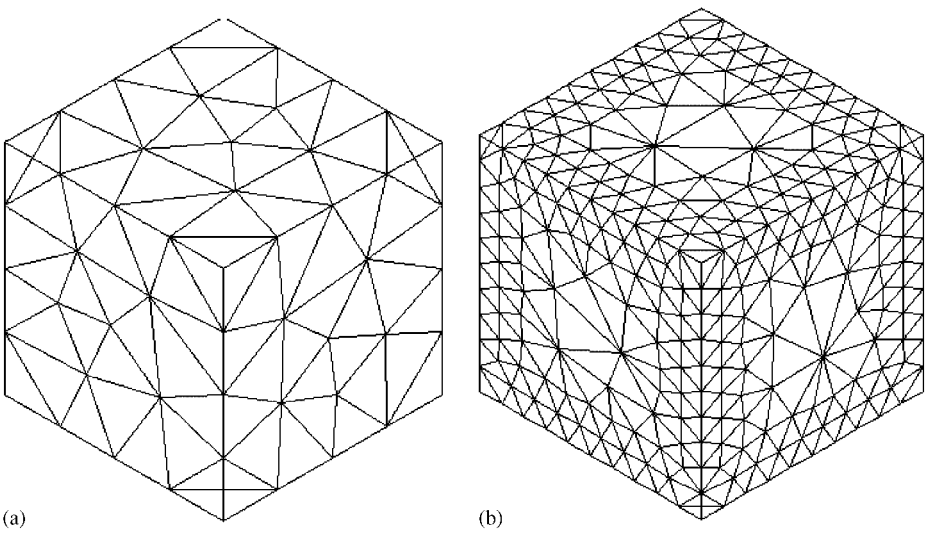

Figure 11. Scattering of a plane electromagnetic wave by a cube of edge length 1λ: view of the surface meshes employed.

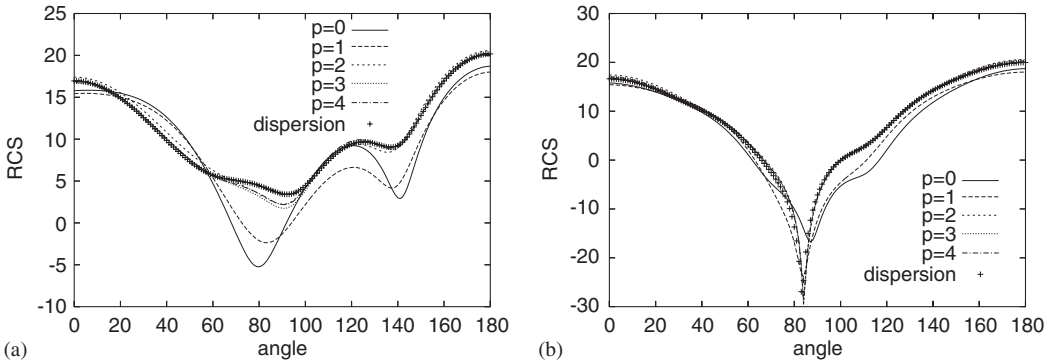

Figure 12. Scattering of a plane electromagnetic wave by a cube of edge length 1λ: distribution of the bistatic RCS, computed with uniform increase of polynomial order and with a polynomial order distribution obtained from the dispersion relationship, for the uniform mesh for: (a) the vertical polarization; and (b) the horizontal polarization.

RCS distribution determined by using uniform p refinement. The small differences which occur are attributed to the better resolution of singularities on the geometrically refined mesh. A comparison of the corresponding number of unknowns in each of these cases is shown in Table III. The table illustrates that a large saving in the number of unknowns can be achieved by using an appropriate non-uniform distribution of p at the outset. An indication of

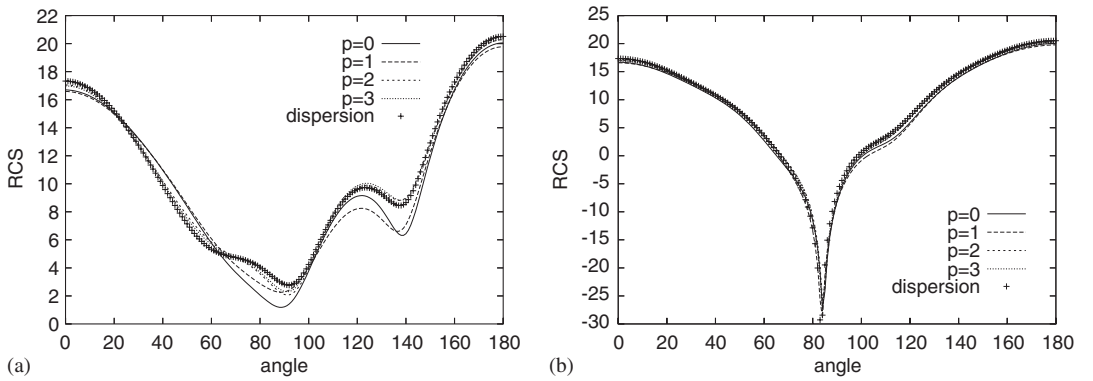

Figure 13. Scattering of a plane electromagnetic wave by a cube of edge length 1λ: distribution of the bistatic RCS, computed with uniform increase of polynomial order and with a polynomial order distribution obtained from the dispersion relationship, for the geometrically refined mesh for: (a) the vertical polarization; and (b) the horizontal polarization.

Table III. The number of unknowns produced on the uniform mesh and on the geometrically refined mesh, when both uniform p refinement and the non-uniform distribution of p given by the dispersion relationship are used.

	Uniform mesh	Geometrically refined mesh
$p=0$	3061	8431
$p=1$	6122	16 862
$p=2$	23 637	69 315
$p=3$	59 896	180 748
$p=4$	121 730	—
Dispersion	59 815	98 503

the manner in which Algorithm 1 operates may be gained from Figure 14, which illustrates the computed non-uniform distribution of p on the surface of the scatterer, for the graded mesh. The smaller elements closer to the edges and corners are allocated a lower order than the larger elements away from these regions. The bistatic RCS distributions, computed with the non-uniform distribution of p on the two meshes, are compared in Figure 15. It can observed that using the geometrically refined mesh leads to a more accurate prediction of the RCS distribution. The distribution of contours of the scattered field components, computed on the surface of the cube on the geometrically refined mesh, are shown in Figure 16.

5.3. Monostatic scattering by a 1λ *NASA almond*

The simulation of scattering by a perfect electrical conducting NASA almond is often used as a test case when analysing the performance of numerical algorithms for the solution of Maxwell's equations, with the singularity at the tip of the almond making this a challenging

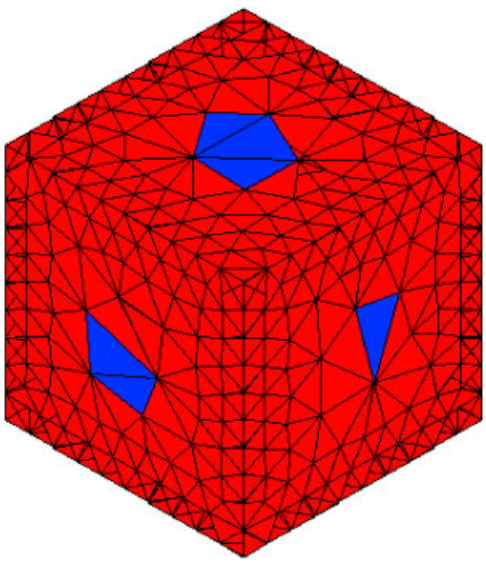

Figure 14. Scattering of a plane electromagnetic wave by a cube of edge length 1λ: the non-uniform distribution of p, on the surface elements, obtained from the dispersion relationship on the graded mesh; the colours red and blue represent elements of order $p=2$ and $p=3$, respectively.

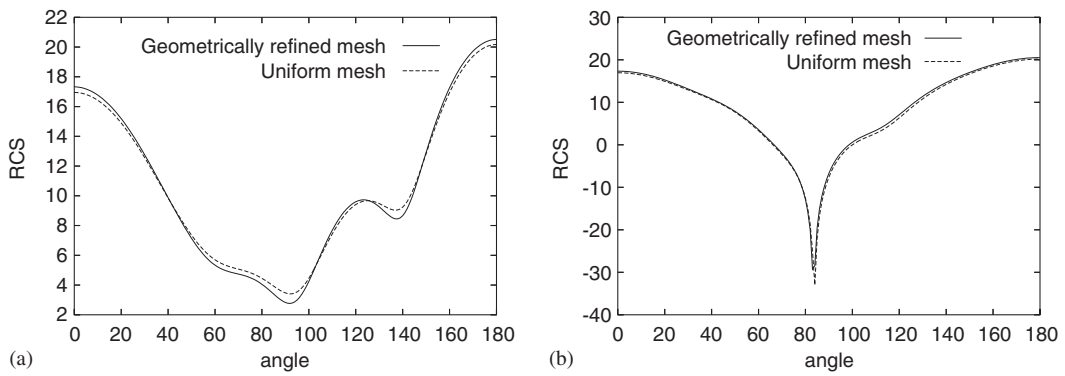

Figure 15. Scattering of a plane electromagnetic wave by a cube of edge length 1λ: the distribution of the bistatic RCS for: (a) the vertical polarization; and (b) the horizontal polarization, computed in each case with the dispersion relationship on the uniform and the geometrically refined meshes.

example. The mesh employed for the computation has 4723 tetrahedral elements and a view of the surface discretization is given in Figure 17. To compare our results with that of experimental observations, we set up a series of $N_{\text{inc}}+1$ incident waves $\mathbf{E}^{\text{inc}}(\phi_i)$, $i=0,\ldots,N_{\text{inc}}$ where we select the directions as $\theta=\pi/2$ and $\phi_i=\mathrm{i}\delta\phi$, where $\delta\phi=\pi/N_{\text{inc}}$ and we take $E_\theta^{\text{inc}}=-1$,

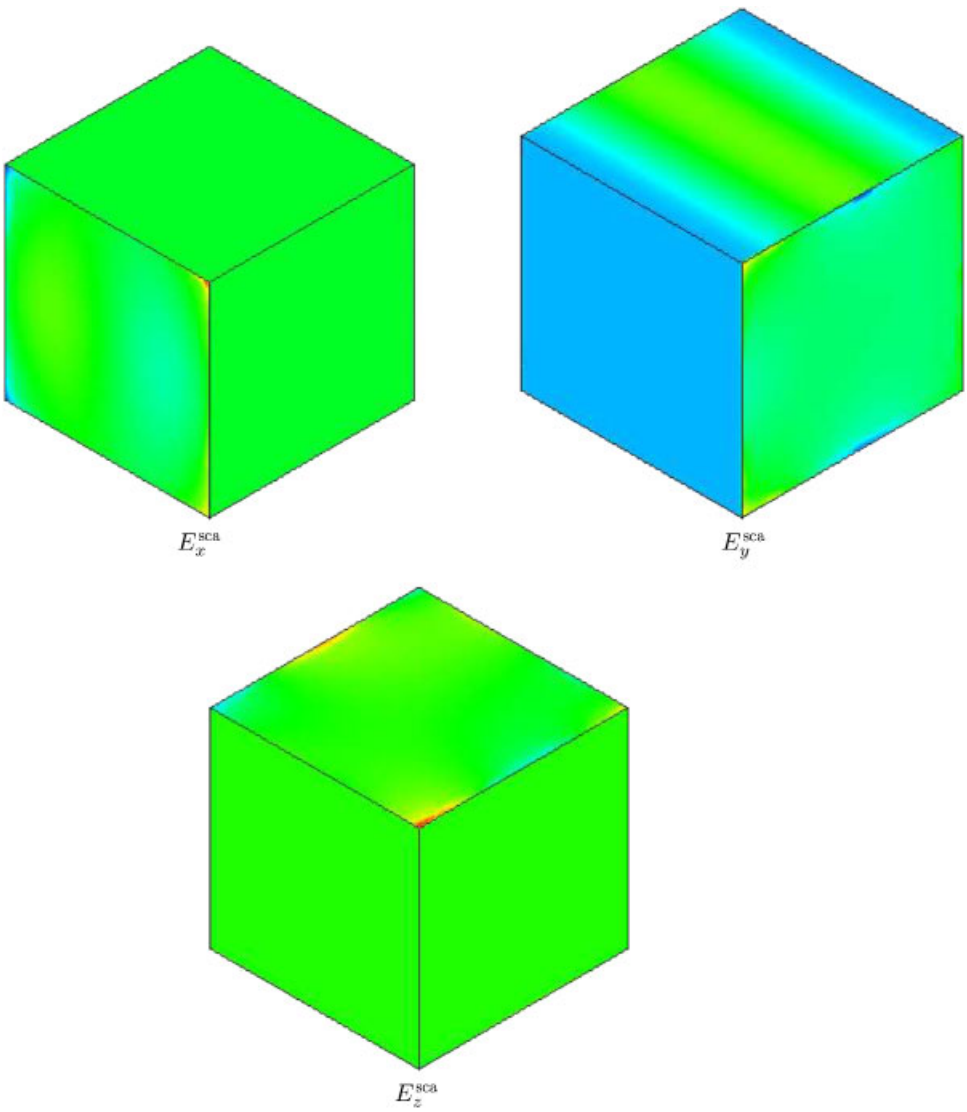

Figure 16. Scattering of a plane electromagnetic wave by a cube of edge length 1λ: the computed contours of E_x^{sca}, E_y^{sca} and E_z^{sca} on the cube surface.

$E_\phi^{\mathrm{inc}} = 0$ for vertically polarized waves and $E_\theta^{\mathrm{inc}} = 0$, $E_\phi^{\mathrm{inc}} = 1$ for horizontally polarized waves. A non-uniform distribution of polynomial order is employed, with the order for each element being determined by Algorithm 1. Using the same angles, and the scattered field corresponding to each of the incident waves, enables both the vertical and horizontally polarized monostatic RCS distributions to be computed. The computed and experimental RCS distributions are

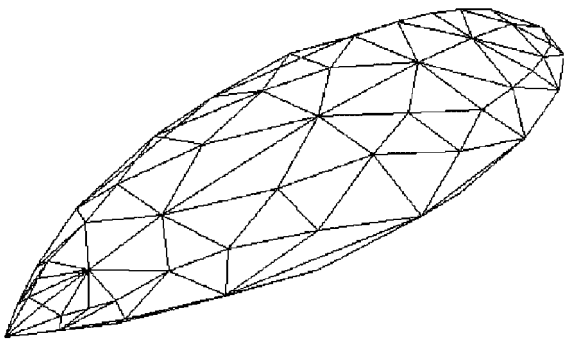

Figure 17. Scattering of a plane electromagnetic wave by an almond of length 1λ: view of the surface mesh employed.

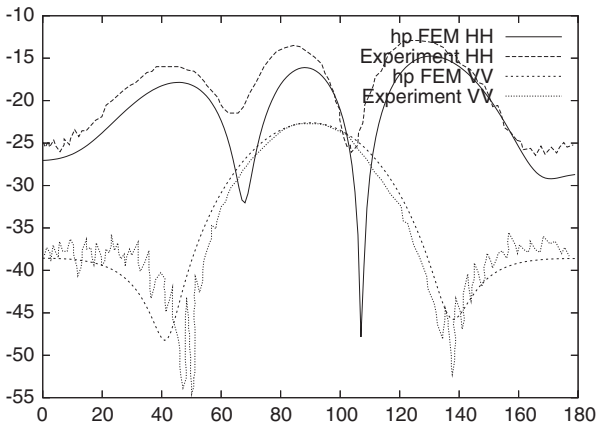

Figure 18. Scattering of a plane electromagnetic wave by an almond of length 1λ: comparison of the computed and experimentally observed distribution of the monostatic RCS.

compared in Figure 18. It can be seen that excellent agreement is achieved for the vertical polarization of the RCS, although differences occur between the computed distribution of the horizontal polarization and the profile given by the experimental results. Taflove and Hagness [26] reported similar differences in the horizontal polarization of the RCS when a finite difference scheme time domain scheme was used. In this work, they attributed the differences to inaccuracies in ABCs.

5.4. Monostatic scattering by a $1.75\lambda \times 1\lambda$ *flat plate*

Scattering of a plane wave by a perfect electrical conducting plate offers further possibilities for the validation of the solution method, as solutions for this problem may also be obtained using physical optics and diffraction theory. These two methods lead to different monostatic

RCS distributions, with the distribution of the physical optics approximation being accurate for small angles. To make comparisons possible with these theories, we set up a series of $N_{\text{inc}}+1$ incident waves $\mathbf{E}^{\text{inc}}(\theta_i)$, $i=0,\ldots,N_{\text{inc}}$ where we select the directions as $\phi=0$ and $\theta_i=-\pi/2+\text{i}\delta\theta$, where $\delta\theta=\pi/N_{\text{inc}}$ and we take $E_\theta^{\text{inc}}=0$, $E_\phi^{\text{inc}}=1$ for vertically polarized waves and $E_\theta^{\text{inc}}=-1$, $E_\phi^{\text{inc}}=0$ for horizontally polarized waves. For an infinitely thin plate in the xy plane, the physical optics monostatic RCS distribution is [36]

$$\sigma_{VV}=\sigma_{HH}=\frac{4\pi A^2}{\lambda^2}\cos^2\theta\left(\frac{\sin kau}{kau}\right)^2\left(\frac{\sin kav}{kav}\right)^2 \tag{49}$$

for the incident waves defined above. Here, $A=ab$ is the area of the plate, $a=1.75\lambda$ and $b=\lambda$ are the dimensions of the plate in the x and y directions respectively. Furthermore, u and v are the direction cosines of the vector $\mathbf{r}=(\sin\theta\cos\phi,\sin\theta\sin\phi,\cos\theta)$ to the x and y coordinate directions. Using diffraction theory, the corresponding distributions for the same problem are given by [37]

$$\begin{aligned}\sigma_{VV}=\frac{4b^2}{\pi}\Bigg|&\left[\cos(2\omega a\sin\theta)-\frac{\text{i}\sin(2\omega a\sin\theta)}{\sin\theta}\right]\\&-\frac{\text{e}^{\text{i}2\omega a-\text{i}(\pi/4)}}{\sqrt{2\pi}(2\omega a)^{3/2}}\left[\frac{1}{\cos\theta}+\frac{\text{e}^{\text{i}2\omega a-\text{i}(\pi/4)}}{4\sqrt{2\pi}(2\omega a)^{3/2}}\left(\frac{(1+\sin\theta)\text{e}^{-\text{i}2\omega a\sin\theta}}{(1+\theta)^2}+\frac{(1-\sin\theta)\text{e}^{-\text{i}2\omega a\sin\theta}}{(1+\theta)^2}\right)\right]\\&\times\left[1-\frac{\text{e}^{\text{i}4\omega a-\text{i}(\pi/2)}}{8\pi(2\omega a)^3}\right]^{-1}\Bigg|^2\end{aligned} \tag{50}$$

and

$$\begin{aligned}\sigma_{HH}=\frac{4b^2}{\pi}\Bigg|&\left[\cos(2\omega a\sin\theta)+\frac{\text{i}\sin(2\omega a\sin\theta)}{\sin\theta}\right]\\&-\frac{\text{e}^{\text{i}2\omega a+\text{i}(\pi/4)}}{\sqrt{2\pi}(2\omega a)^{1/2}}\left[\frac{1}{\cos\theta}-\frac{\text{e}^{\text{i}2\omega a+\text{i}(\pi/4)}}{4\sqrt{2\pi}(2\omega a)^{1/2}}\left(\frac{\text{e}^{-\text{i}2\omega a\sin\theta}}{1-\theta}+\frac{\text{e}^{\text{i}2\omega a\sin\theta}}{1+\theta}\right)\right]\\&\times\left[1-\frac{\text{e}^{\text{i}4\omega a+\text{i}(\pi/2)}}{2\pi(2\omega a)}\right]^{-1}\Bigg|^2\end{aligned} \tag{51}$$

These distributions become invalid at $\theta=\pm\pi/2$ and, due to the assumptions made, they become more accurate as the frequency increases. For the *hp* finite element solution of this problem, a mesh of 5051 tetrahedral elements is used and a view of the surface discretization is given in Figure 19. A non-uniform distribution of polynomial order is employed, with the order for each element being determined by Algorithm 1. The computed monostatic RCS distributions are compared with the results of physical optics and diffraction theory in Figure 20.

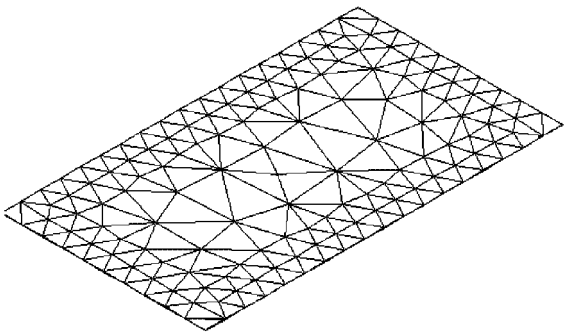

Figure 19. Scattering of a plane electromagnetic wave by a $1.75\lambda \times 1\lambda$ plate: a view of the surface mesh employed.

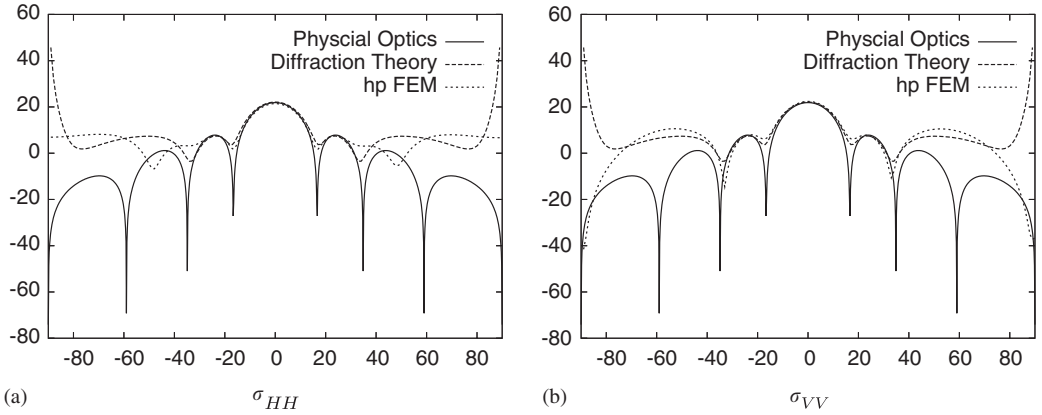

Figure 20. Scattering of a plane electromagnetic wave by a $1.75\lambda \times 1\lambda$ plate: comparison between the computed distribution of the monostatic RCS with the distributions obtained from both physical optics and diffraction theory.

For both polarizations, it can be observed that the physical optics solution agrees with diffraction theory and the numerical solution only for very small angles. Beyond these angles, the solution obtained by physical optics becomes invalid. The diffraction theory solution exhibits excellent agreement with the finite element solution for angles less than about 40°. For larger angles, the profiles are similar, but the geometric diffraction theory tends to infinity as θ tends to 90°. The differences between the finite element solution and diffraction theory are attributed to the approximations inherent in the diffraction theory model. Indeed Ross [37] observes differences in the theory and experimental results for angles $|\theta| \geqslant 40°$. In Figure 21 we show the computed scattered field corresponding to the incident wave with the direction $\theta = -\pi/2,\ \phi = 0$.

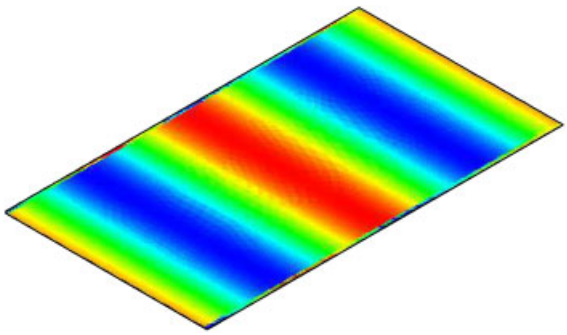

Figure 21. Scattering of a plane electromagnetic wave by a $1.75\lambda \times 1\lambda$ plate: computed contours of the scattered field E_y^{sca} on the plate surface.

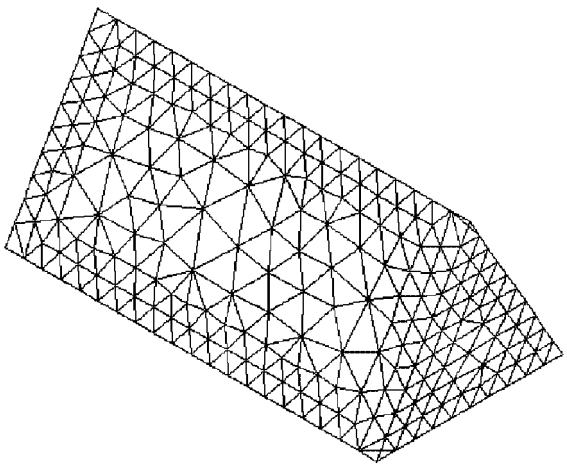

Figure 22. Scattering of a plane electromagnetic wave by a $2.5\lambda \times 5\lambda$ triangular cylinder: view of the surface mesh employed.

5.5. Monostatic scattering by a $2.5\lambda \times 5\lambda$ triangular cylinder

For the final example, electromagnetic wave by a cylinder, of equilateral triangular cross-section and side length $a = 2.5\lambda$. The length of the cylinder is $b = 5\lambda$. A mesh of 10 023 tetrahedra is employed and a view of the surface discretization is shown in Figure 22. We consider a series of $N_{\text{inc}} + 1$ incident waves $\mathbf{E}^{\text{inc}}(\theta_i)$, $i = 0, \ldots, N_{\text{inc}}$ where we select the directions as $\phi = 0$ and $\theta_i = -\pi/2 + \mathrm{i}\delta\theta$, where $\delta\theta = \pi/N_{\text{inc}}$ and we take $E_\theta^{\text{inc}} = 0$, $E_\phi^{\text{inc}} = 1$ for vertically polarized waves and $E_\theta^{\text{inc}} = -1$, $E_\phi^{\text{inc}} = 0$ for horizontally polarized waves. A non-uniform distribution of polynomial order is employed. The computed monostatic RCS distributions, for the horizontal and vertical polarizations, are shown in Figure 23. A view of the computed contours of the scattered field component E_z^{sca} on the surface of the cylinder is shown in Figure 24 for the incident wave with the direction $\theta = -\pi/2$, $\phi = 0$.

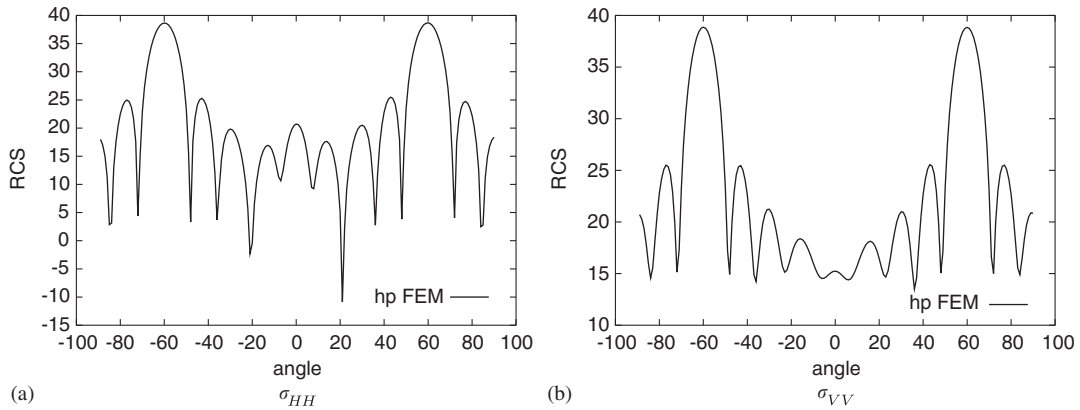

Figure 23. Scattering of a plane electromagnetic wave by a $2.5\lambda \times 5\lambda$ triangular cylinder: computed distributions of the monostatic RCS for both the horizontal and vertical polarizations.

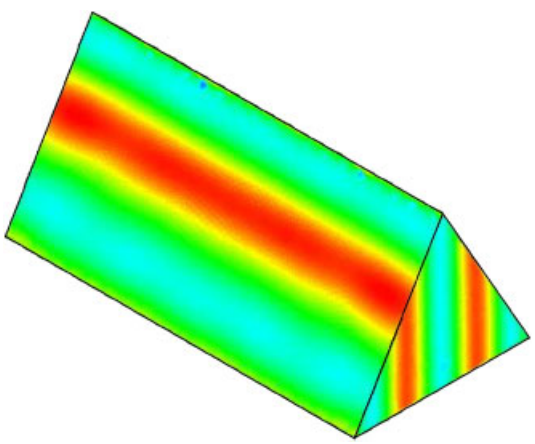

Figure 24. Scattering of a plane electromagnetic wave by a $2.5\lambda \times 5\lambda$ triangular cylinder: computed contours of the scattered field E_z^{sca} on the surface of the cylinder.

6. CONCLUSIONS

In this paper, we have described an approach for solving electromagnetic scattering problems in three dimensions using *hp* version **H**(curl) conforming finite elements based on tetrahedral meshes. For general simulations, we have relied upon the use of a dispersion relationship [28] to provide a non-uniform distribution of polynomial order through the mesh. The complex system of linear equations is solved by using the Pardiso library [29, 30]. A number of numerical examples have been presented which demonstrate the performance of the approach.

Currently, the approach is being extended to include the use of automatic adaptive refinement, through error estimation, and the improvement of the monostatic RCS calculation, through the use of reduced-order models [38].

REFERENCES

1. Nédélec JC. Computation of eddy currents on a surface in $\mathbb{R}^3$ by finite element methods. *SIAM Journal of Numerical Analysis* 1978; **15**:580–594.
2. Nédélec JC. Mixed elements in $\mathbb{R}^3$. *Numerische Mathematik* 1980; **35**:315–341.
3. Nédélec JC. A new family of mixed elements in $\mathbb{R}^3$. *Numerische Mathematik* 1986; **50**:57–81.
4. Ledger PD, Morgan K. The application of the *hp*-finite element method to electromagnetic problems. *Archives of Computational Methods in Science and Engineering* 2005; **12**:235–302.
5. Ledger PD, Morgan K, Hassan O, Weatherill NP. Arbitrary order edge elements for electromagnetic scattering simulations using hybrid meshes and a PML. *International Journal for Numerical Methods in Engineering* 2002; **55**:339–358.
6. Ainsworth M, Coyle J. Hierarchic *hp*-edge element families for Maxwell's equations on hybrid quadrilateral/triangular meshes. *Computer Methods in Applied Mechanics and Engineering* 2001; **190**:6709–6733.
7. Berenger J-P. A perfectly matched layer for the absorption of electromagnetic waves. *Journal of Computational Physics* 1994; **114**:185–200.
8. Ledger PD. An *hp*-adaptive finite element procedure for electromagnetic scattering problems. *Ph.D. Thesis*, Department of Civil Engineering, University of Wales, Swansea, 2002.
9. Ledger PD, Peraire J, Morgan K, Hassan O, Weatherill NP. Efficient highly accurate *hp*-adaptive finite element computations of the scattering width output of Maxwell's equations. *International Journal for Numerical Methods in Fluids* 2003; **43**:953–978.
10. Ledger PD, Morgan K, Peraire J, Hassan O, Weatherill NP. The development of an *hp* adaptive finite element procedure for electromagnetic scattering problems. *Finite Elements in Analysis and Design* 2003; **39**:751–764.
11. Ainsworth M, Coyle J. Hierarchic finite element basis on unstructured tetrahedral meshes. *International Journal for Numerical Methods in Engineering* 2003; **58**:2103–2130.
12. Ainsworth M, Coyle J, Ledger PD, Morgan K. Computation of Maxwell eigenvalues using higher order edge elements. *IEEE Transactions on Magnetics* 2003; **39**:2149–2153.
13. Coyle J, Ledger PD. Evidence of exponential convergence in the computation of Maxwell eigenvalues. *Computer Methods in Applied Mechanics and Engineering* 2004; **194**:587–604.
14. Ledger PD, Morgan K, Hassan O. Frequency and time domain electromagnetic scattering simulations employing higher order edge elements. *Computer Methods in Applied Mechanics and Engineering* 2005; **194**:105–125.
15. Rachowicz W, Zdunek A. An *hp* adaptive finite element method for scattering problems in electromagnetics. *International Journal for Numerical Methods in Engineering* 2005; **62**:1226–1249.
16. Zdunek A, Rachowicz W. A goal orientated *hp* adaptive finite element approach to radar scattering problems. *Computer Methods in Applied Mechanics and Engineering* 2005; **194**:657–674.
17. Weatherill NP, Marchant MJ, Hassan O, Marcum DL. Grid adaption using a distribution of sources applied to inviscid compressible flow simulations. *International Journal for Numerical Methods in Fluids* 1994; **19**: 739–764.
18. Jin J. *The Finite Element Method in Electromagnetics*. Wiley: New York, 1993.
19. Volakis JL, Chatterjee A, Kemplel LC. *Finite Element Method for Electromagnetics*, *Antennas*, *Microwave Circuits and Scattering Applications*. IEEE Press: New York, 1998.
20. Givoli D. *Numerical Methods for Problems in Infinite Domains*. Elsevier: Amsterdam, 1992.
21. Givoli D. Recent advances in the DtN FE method. *Archives in Computational Methods in Engineering* 1999; **6**:71–116.
22. Bettess P. *Infinite Elements*. Penshaw Press: Sunderland, 1992.
23. Sacks ZS, Kingsland DM, Lee R, Leee JF. A perfectly matched anisotropic absorber for use as an absorbing boundary condition. *IEEE Transactions on Antennas and Propagation* 1995; **43**:1460–1463.
24. Kuzuoglu M, Mittra R. Investigation of non-planar perfectly matched absorber for finite element mesh truncation. *IEEE Transactions on Antennas and Propagation* 1997; **45**:474–486.
25. Demkowicz L, Pal M. An infinite element for Maxwell's equations. *Computer Methods in Applied Mechanics and Engineering* 1998; **164**:77–94.
26. Taflove A, Hagness SC. *Computational Electrodynamics*. Artech House: Boston, London, 2000.
27. Collino F, Monk P. The perfectly matched layer in curvilinear coordinates. *SIAM Journal of Scientific Computing* 1998; **19**:2061–2090.
28. Ainsworth M. Discrete properties of high order Nédélec/edge element approximation of the time-harmonic Maxwell equations. *Philosophical Transactions of the Royal Society Series A* 2004; **362**:471–493.

29. Schenk O, Gärtner K. Solving unsymmetric sparse systems of linear equations with PARDISO. *Journal of Future Generation Computer Systems* 2004; **20**(3):475–487.
30. Schenk O, Gärtner K, Fichtner W. Scalable parallel sparse factorization with left-right looking strategy on shared memory multiprocessor. *BIT Numerical Mathematics* 2000; **40**(1):158–176.
31. Karypis G, Kumar V. A fast and high quality multilevel scheme for partitioning irregular graphs. *SIAM Journal on Scientific Computing* 1998; **20**:359–392.
32. Gould NIM, Hu Y, Scott JA. A numerical evaluation of sparse direct solvers for the solution of large sparse symmetric systems of linear equations. *Technical report*, Council for the Central Laboratory of Research Councils, 2005.
33. Monk P, Suli E. The adaptive computation of far field patterns by *a posteriori* error estimation of linear functionals. *SIAM Journal of Numerical Analysis* 1998; **36**:251–274.
34. Monk P. The near to far field transformation. *The International Journal for Computation and Mathematics in Electrical and Electronic Engineering* 1995; **14**:41–56.
35. Parott K, Monk P. Phase accuracy and improved farfield estimates for 3-D edge elements on tetrahedral meshes. *Journal of Computational Physics* 2001; **170**:614–641.
36. Jenn DC. *Radar and Laser Cross Section Engineering*. AIAA Education Series: Washington, 1995.
37. Ross SW. *Radar Cross Sections of Complex Objects*. IEEE Press: New York, 1990.
38. Ledger PD, Peraire J, Morgan K, Hassan O, Weatherill NP. Parameterised electromagnetic scattering solutions for a range of incident wave angles. *Computer Methods in Applied Mechanics and Engineering* 2004; **193**: 3587–3605.

